V European Conference on Computational Fluid Dynamics
ECCOMAS CFD 2010
J. C. F. Pereira and A. Sequeira (Eds)
Lisbon, Portugal, 14–17 June 2010

UNSTEADY VISCOUS ANALYSIS OF LOW-RE GUST-AIRFOIL INTERACTION

Vladimir Golubev[*] and Miguel Visbal[†]

[*]Florida Center for Advanced Aero Propulsion
Embry-Riddle Aeronautical University
Daytona Beach, Florida, USA
e-mail: Vladimir.Golubev@erau.edu

[†]Air Force Research Laboratory
Wright-Patterson AFB, Ohio, USA
e-mail: Miguel.Visbal@wpafb.af.mil

Key words: High-Accuracy, Low-Re, MAV, Gust, Pitching, Airfoil Response

Abstract. *A parametric numerical study is implemented to examine the unsteady aerodynamic responses to incident 1D and 2D time-harmonic vortical gusts. The analysis is focused on the low-Re number unsteady flows typical of MAV applications in which a gust encounter can induce a particularly significant aerodynamic and aeroelastic response. Efficient models are developed to introduce the flow perturbations inside the computational domain through the source terms in the governing momentum equations. High-accuracy Navier-Stokes simulations are conducted for SD7003 airfoil installed at the angles of attack of 4^0 and 8^0 in the laminar flow regime with M_∞ =0.1 and Re=10,000. The varied parameters include the gust reduced frequency and amplitude. The gust aerodynamic response is examined in comparison with results from the corresponding time-harmonic pitching airfoil simulations. The unsteady predictions are matched against theoretical incompressible inviscid solutions revealing the relative dominance of viscous and inviscid effects in the gust and pitching responses for the selected flow regimes.*

1 INTRODUCTION

The current study is motivated by the need to develop an accurate, robust prediction tool for analysis of nonlinear aerodynamic and aeroelastic responses of a fixed-wing Micro Air Vehicle (MAV) to impinging vortical unsteady flow perturbations (gusts). Despite a certain degree of maturity reached by low-Re aerodynamics research in recent years [1, 2], very few studies examined the effects of gust impact on the MAV wing aerodynamic performance. On the other hand, while even small wind gusts and atmospheric turbulence may be of minor significance to larger, heavier aircraft, they can be devastating for MAV stability and control.

As reviewed, e.g., in Ref. [3], most experimental and numerical works in the area of MAV unsteady aerodynamics considered canonical pitch-ramp and plunge airfoil maneuvers in order to systematically examine patterns of separated vortical flow dynamics, especially including the aerodynamically critical processes of laminar separation bubble (LSB) formation and burst and related transition phenomena. A few recent studies [4-7] considered time-harmonic oscillations of the free-stream velocity which primarily impacts the dynamics of the airfoil boundary layer transition and causes hysteresis in airfoil aerodynamic characteristics at low Re numbers.

In this work, we focus on the airfoil response induced by the convected *upwash* component of the unsteady, non-uniform upstream flowfield which directly affects the unsteady aerodynamic loading. In particular, the gust interaction model producing the time-harmonic gust-induced variations of the effective airfoil angle-of-attack is examined. For the transverse 1D gust, the numerical predictions are compared against the classical linearized inviscid, incompressible unsteady aerodynamic theory in which the corresponding flat-plate response to such disturbance is analytically described by Sears' solution. Furthermore, both numerical (viscous) and analytical (inviscid) gust response predictions are compared against corresponding solutions obtained for the pitching airfoil with equivalent induced upwash velocity component. The results of the parametric study conducted for SD7003 airfoil (used as a benchmark in the majority of recent low-Re studies) elucidate relative significance of viscous and inviscid effects in the MAV airfoil unsteady aerodynamic response for a range of gust parameters including gust amplitude and frequency. Importantly, the study reveals the major physical differences existing between the gust and pitching unsteady airfoil responses.

2 GOVERNING EQUATIONS AND NUMERICAL MODEL

The employed high-accuracy numerical code FDL3DI [8] solves a set of compressible Navier-Stokes equations represented in strong, conservative, time-dependent form in the generalized curvilinear computational coordinates (ξ,η,ζ,τ) transformed from the physical coordinates (x,y,z,t),

$$\frac{\partial}{\partial\tau}\left(\frac{\vec{Q}}{J}\right)+\frac{\partial\vec{F}_i}{\partial\xi}+\frac{\partial\vec{G}_i}{\partial\eta}+\frac{\partial\vec{H}_i}{\partial\zeta}+\frac{1}{\mathrm{Re}}\left[\frac{\partial\vec{F}_v}{\partial\xi}+\frac{\partial\vec{G}_v}{\partial\eta}+\frac{\partial\vec{H}_v}{\partial\zeta}\right]=\vec{S} \tag{1}$$

The solution vector $\vec{Q}=(\rho,\rho u,\rho v,\rho w,\rho e)$ is defined in terms of the flow density ρ, Cartesian flow velocity components (u, v, w), and flow specific energy,

$$e=\frac{T}{\gamma(\gamma-1)M_\infty^2}+\frac{1}{2}(u^2+v^2+w^2)$$

with assumed perfect gas relationship. The other variables in Eq. (1) include the inviscid flux vectors defined by

$$\vec{F}_i = \begin{bmatrix} \rho\hat{u} \\ \rho u\hat{u} + \hat{\xi}_x p \\ \rho v\hat{u} + \hat{\xi}_y p \\ \rho w\hat{u} + \hat{\xi}_z p \\ (\rho e + p)\hat{u} - \hat{\xi}_t p \end{bmatrix}, \quad \vec{G}_i = \begin{bmatrix} \rho\hat{v} \\ \rho u\hat{v} + \hat{\eta}_x p \\ \rho v\hat{v} + \hat{\eta}_y p \\ \rho w\hat{v} + \hat{\eta}_z p \\ (\rho e + p)\hat{v} - \hat{\eta}_t p \end{bmatrix}, \quad \vec{H}_i = \begin{bmatrix} \rho\hat{w} \\ \rho u\hat{w} + \hat{\zeta}_x p \\ \rho v\hat{w} + \hat{\zeta}_y p \\ \rho w\hat{w} + \hat{\zeta}_z p \\ (\rho e + p)\hat{w} - \hat{\zeta}_t p \end{bmatrix}$$

the transformation Jacobian, $J = \partial(\xi,\eta,\zeta,\tau)/\partial(x,y,z,t)$, the metric quantities defined, e.g., as $\hat{\xi}_x = (J^{-1})\partial\xi/\partial x$, etc., and the transformed flow velocity components,

$$\hat{u} = \hat{\xi}_t + \hat{\xi}_x u + \hat{\xi}_y v + \hat{\xi}_z w$$
$$\hat{v} = \hat{\eta}_t + \hat{\eta}_x u + \hat{\eta}_y v + \hat{\eta}_z w$$
$$\hat{w} = \hat{\zeta}_t + \hat{\zeta}_x u + \hat{\zeta}_y v + \hat{\zeta}_z w$$

The viscous flux vectors, $\vec{F}_v$, $\vec{G}_v$ and $\vec{H}_v$, are defined, e.g., in Ref. [9], while $\vec{S}$ represents the source term which in the current work generates an unsteady, incompressible vortical perturbation upstream of the wing section. All the flow variables are normalized by their respective reference freestream values except for pressure which is nondimensionalized by $\rho_\infty u_\infty^2$.

Note that the governing equations are represented in the original unfiltered form used unchanged in the laminar, transitional or fully turbulent regions of the flow. Refs [10, 11] provide further details on the code's Implicit LES (ILES) procedure in which a high-order low-pass filter operator is applied to the dependent variables during the solution process, in contrast to the standard LES addition of sub-grid stress (SGS) and heat flux terms. The resulting filter selectively damps the evolving poorly resolved high-frequency content of the solution.

The code employs a finite-difference approach to discretize the governing equations, with all the spatial derivatives obtained using the high-order compact-differencing schemes from Ref. [12]. For the wing section computations of the current paper, a sixth-order scheme is used. At boundary points, higher-order one-sided formulas are utilized which retain the tridiagonal form of the scheme. In order to ensure that the Geometric Conservation Law (GCL) is satisfied, the time metric terms are evaluated employing the procedures described in detail in Ref. [8]. Finally, the time marching is accomplished by incorporating a second-order iterative, implicit approximately-factored scheme.

3 TIME-HARMONIC GUST SOURCE MODEL

The classical configuration of the time-harmonic gust-airfoil interaction problem shown in Fig. 1 serves as one of the benchmarks in computational fluid dynamics [13]. It generally models the unsteady response of a lifting surface to the incident flow turbulence or upstream-generated flow unsteadiness. Such velocity field may be

described in terms of the following Fourier spectrum containing various perturbation frequencies and wave numbers,

$$u'(\vec{x},t) = \mathrm{Re}\{\int_{\omega}\sum_{\vec{k}} A_{\vec{k}}(\vec{x})\exp[i(\vec{k}\cdot\vec{x}-\omega t)]\}$$

For numerical simulations, a single harmonic of the two-dimensional vortical perturbation velocity is selected, described in the form,

$$\begin{aligned} u_g &= \varepsilon_u \cos(\alpha x + \beta y - \omega_g t) \\ v_g &= \varepsilon_v \cos(\alpha x + \beta y - \omega_g t) \end{aligned}, \qquad (2)$$

where the gust component amplitudes are,

$$\varepsilon_u = -\left(\frac{\varepsilon_g \beta u_\infty}{\sqrt{\alpha^2+\beta^2}}\right), \qquad \varepsilon_v = \left(\frac{\varepsilon_g \alpha u_\infty}{\sqrt{\alpha^2+\beta^2}}\right), \qquad (3)$$

ε_g is the gust intensity relative to the mean flow, α and β are the gust wave numbers in the x and y directions, respectively, $k_g = \omega_g c/2u_\infty$ is the imposed gust reduced frequency, u_∞ is the convective freestream velocity, and c is the airfoil chord. Note that $\alpha = \omega_g / u_\infty$ and $\beta = \alpha \tan\chi$, where χ is the angle between the normal vector of the gust phase front and the x-axis.

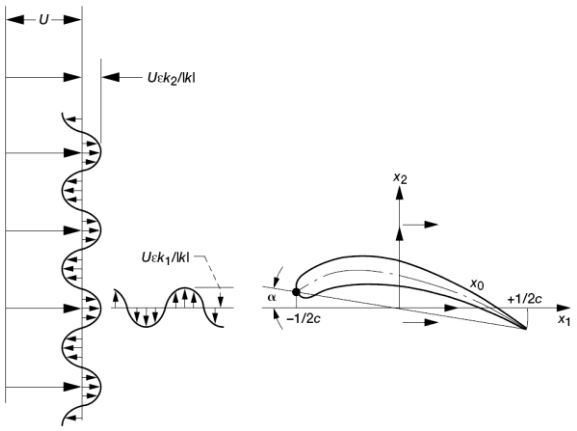

Figure 1: Gust-airfoil interaction problem.

The approach proposed in this work to generate a 2D gust inside the computational domain extends the analysis of Ref. [14] where the analytical 1D gust source was developed. The method avoids imposing the proper vortical flow disturbance at the upstream boundary [15, 16], and allows using stretched computational grids throughout the farfield to minimize spurious reflections.

First, we assume that the gust source is located in a region of uniform flow aligned with the x-direction, and that the interactions between the gust and other waves are negligible. Furthermore, since the gust to be generated downstream of the source region is incompressible and vortical of the form (2), the source terms should only be added to the momentum equations in (1). To this end, to obtain the required solution for $\vec{S} = (s_{u,} s_v)$, we examine the gust momentum equations,

$$\begin{aligned}\frac{\partial u_g}{\partial t}+u_\infty\frac{\partial u_g}{\partial x}&=s_u\\ \frac{\partial v_g}{\partial t}+u_\infty\frac{\partial v_g}{\partial x}&=s_v\end{aligned} \tag{4}$$

Note that, in order to satisfy the divergence-free condition for the incompressible gust, the source components are constrained by $\partial s_u/\partial x+\partial s_v/\partial y=0$. We then seek the solution in the form,

$$\begin{aligned}s_u(x,y,t)&=\beta Kg(x)\cos(\omega_g t-\beta y+\psi_0)\\ s_v(x,y,t)&=Kg'(x)\sin(\omega_g t-\beta y+\psi_0)\end{aligned}, \tag{5}$$

where g'(x)=dg/dx and ψ_0 and K are constants. The solution is obtained in the complex plane where (4) reduces to

$$\begin{aligned}\frac{d\tilde{u}_g}{dx}+i\alpha\tilde{u}_g&=\frac{\beta}{u_\infty}Kg(x)\\ \frac{d\tilde{v}_g}{dx}+i\alpha\tilde{v}_g&=-\frac{i}{u_\infty}Kg'(x)\end{aligned}, \tag{6}$$

and

$$\begin{aligned}u_g(x,y,t)&=\Re[\tilde{u}_g(x)\exp\{i(\omega_g t-\beta y+\psi_0)\}]\\ v_g(x,y,t)&=\Re[\tilde{v}_g(x)\exp\{i(\omega_g t-\beta y+\psi_0)\}]\end{aligned}$$

Focusing for the moment on the first equation in (6), the solution can be expressed as follows,

$$\tilde{u}_g=\frac{\beta K}{u_\infty}\exp(-i\alpha x)\int_{-\infty}^{x}\exp(i\alpha x)g(\sigma)d\sigma,$$

Now, introducing the function g(x),

$$g(x)=\begin{cases}\frac{1}{2}(1+\cos\{b(x-x_s)\}), & |x-x_s|\le\frac{\pi}{b}\\ 0, & |x-x_s|>\frac{\pi}{b}\end{cases},$$

the integration is performed to obtain,

$$\tilde{u}_g=-\frac{\beta K}{\omega_g}\frac{b^2}{(\alpha^2-b^2)}\exp\{-i\alpha(x-x_s)\}\sin(\frac{\omega_g\pi}{u_\infty b})$$

The second equation in (6) can be integrated in a similar fashion. One may then deduce that in order to generate the gust solution of the form (2) downstream of the source region $|x-x_s|\le\pi/b$, we should impose the following source components in the momentum equations from (1),

$$s_u(x,y,t) = \beta K g(x)\lambda(y)\cos(\omega_g t - \beta y - \alpha x_s)$$
$$s_v(x,y,t) = K g'(x)\lambda(y)\sin(\omega_g t - \beta y - \alpha x_s) \quad , \tag{7}$$

where the constant

$$K = \varepsilon_g \frac{\alpha u_\infty^2}{\sqrt{\alpha^2+\beta^2}} \frac{(\alpha^2 - b^2)}{b^2 \sin(\frac{\omega_g \pi}{u_\infty b})}$$

and the function λ(y) is selected to provide a smooth transition in the y-direction to provide a compact region of the uniform gust distribution, e.g.,

$$\lambda(y) = \frac{1}{2}\{\tanh[3(y+y_s)] - \tanh[3(y-y_s)]\}$$

Note that a shear layer is generated in the region where λ(y) varies, but the resulting pressure waves have generally very moderate amplitudes. The generated gust solutions are well-behaved as long as the parameters are selected to avoid very high values of the constant *K*.

To verify the gust source model, the unsteady viscous flow simulations were conducted around a stationary SD7003 airfoil section in the laminar flow regime with M_∞ =0.1 and $\mathrm{Re} = \rho u_\infty c/\mu = 10{,}000$. The results in Fig. 2 are presented for 2D gust (2) with intensity ε_g =0.1, convecting with $\chi = 45^0$ and oscillating with reduced frequency $k_g = 2$. Note that with the code's non-dimensionalization, the gust wavenumbers and frequency are $\alpha = \beta = \omega_g = 2k_g = 4$. A fixed time step of $\Delta t = 5\times10^{-5}$ is chosen, which corresponds to CFL~10. Fig. 2(a) first illustrates the gust vorticity contours, with the box indicating the gust source region.

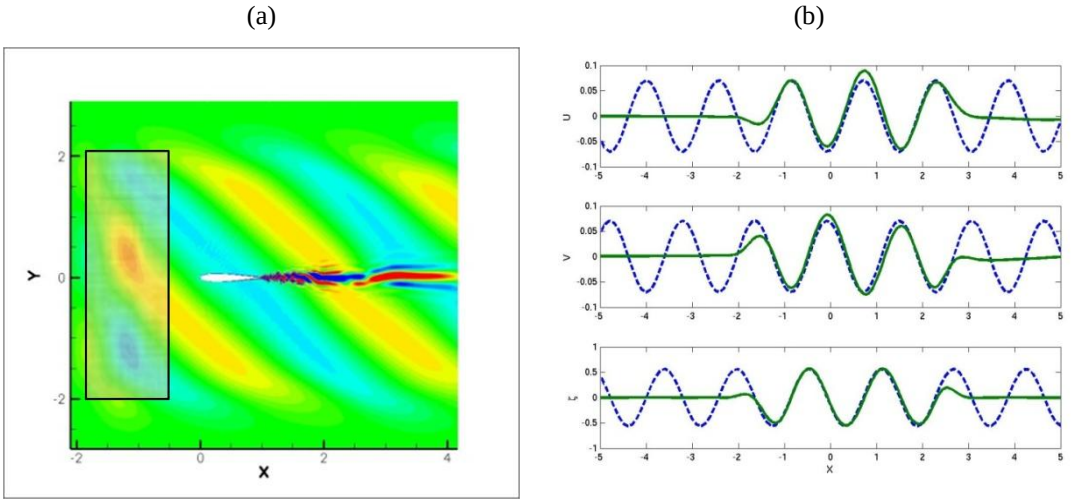

Figure 2: (a) Contour plot for flow vorticity showing the gust evolution and source region with x_s=-1.5, y_s=2, and b=5 (b) Flow velocity components and vorticity along the line y=1, at t=6.

Figure 2(b) shows the comparison of the analytical and numerical predictions for the flow velocity components *u*, *v* and vorticity ς at t=6, obtained along the convection line y=1. Note that the computed velocities (solid lines) deviate from the analytical predictions due to the impact of the potential pressure waves propagating from the

airfoil. However, the vorticity plots match very well. The selected gust source region is used in all subsequent studies.

4 PITCHING AIRFOIL MODEL

For comparison with time-harmonic gust responses, the pitching airfoil motion is prescribed in terms of the harmonic variation of the airfoil angle of attack with frequency ω_{pt} relative to the pitching center x_p,

$$\alpha(t) = \alpha_m \sin \omega_{pt} t + \alpha_0 \tag{8}$$

This variation of the angle of attack translates to the following time-dependent grid motion:

$$X(t) = x_p + (X_0 - x_p)\cos\alpha(t) + Y_0 \sin\alpha(t)$$
$$Y(t) = -(X_0 - x_p)\sin\alpha(t) + Y_0 \cos\alpha(t)$$

where (X_0,Y_0) corresponds to the reference airfoil position at α_0.

5 RESULTS AND DISCUSSION

The current study performs numerical simulations for SD7003 airfoil in the laminar flow regime with M_∞ =0.1 and $\mathrm{Re} = \rho u_\infty c / \mu = 10{,}000$. As before, all variables below are non-dimensionalized by the airfoil chord c, flow density ρ_∞, and flow velocity u_∞. Two cases of the background steady-state flows are considered corresponding to the airfoil installed at the angles of attack $\alpha_0=4^0$ and $\alpha_0=8^0$. The original 649 × 395 × 3 grid generated around SD7003 airfoil was previously employed in Ref [17]. For the current low-Re study, the coarse 327 × 198 × 3 version was carefully tested against the original fine mesh and showed good predictions agreement obtained for flow parameters within the range of interest. To improve the computational efficiency, such mesh was subsequently selected for this parametric study.

A fixed time step with $\Delta t = 2\times10^{-4}$ is chosen for implicit time marching. All results presented here are obtained from the code parallel simulations using ERAU's 262-processor Beowulf Zeus cluster (64-bit, 3.2 GHz Intel Xeon, 4GB RAM systems), with the mesh efficiently partitioned into a set of 32 overlapped blocks assigned to different processors.

The results of unsteady viscous simulations are obtained for 1D ($\beta = 0$ in (2)) and 2D ($\beta = \alpha = \omega_g$ in (2)) time-harmonic gusts generated by the described above momentum source for the gust duration period T_g =10. A detailed comparison with analytical solutions and pitching responses is presented for 1D gust, followed by a review of observed differences between 1D and 2D gust responses. Two gust frequencies are examined corresponding to gust wavelengths $\lambda_g = 2\pi/\omega_g$ =1, 2.5 (non-dimensionalized by the chord), with equivalent pitching airfoil frequencies $\omega_{pt}=2\pi/\lambda_g=2\pi$, $4\pi/5$ in (8). The low-amplitude and high-amplitude gust perturbations are investigated for ε_g =0.07 and ε_g =0.35, with the equivalent upwash velocities produced by the corresponding pitching airfoil motion with $\alpha_m=4^0$ and 20^0.

5.1 Cases with $\alpha_0=4^0$

The time-periodic character of the airfoil unsteady lift responses is clearly observed in Figs. 3 and 4 presenting comparison of 1D gust and pitching responses for low and

high excitation amplitudes, respectively. All the responses eventually transition to the steady-state oscillations following the gust passage or the airfoil return to the original position. The viscous effects are mainly manifested through "wiggles" in the gust response curves especially noticed for low-amplitude cases in Fig. 3 where the induced lift fluctuations are comparable to steady-state levels. Overall, the dominant effect of inviscid forces on time-harmonic flow/airfoil oscillations is confirmed by a close comparison of obtained lift time histories against predictions of the inviscid, incompressible unsteady aerodynamic theory. Presented analytical results include Sears' solution for the thin-airfoil unsteady lift response to impinging sinusoidal transverse gust, and the unsteady lift obtained from Theodorsen's theory for oscillating airfoils (both are summarized, e.g., in Ref. [18]). As expected, the lift deviations from the linearized inviscid theory are more noticeable for the low-amplitude gust response where the viscous effects are more prominent (Fig. 3). An intriguing departure from the linear response is also observed for the high-amplitude case and appears most pronounced for λ_g = 2.5 in Fig. 4(b). In general, the differences in amplitudes of the airfoil time-harmonic responses to transverse gust vs. pitching can be explained based on the arguments from the inviscid incompressible theory. For the higher excitation frequency (λ_g = 1 in Figs. 3-4(a)), the greater circulatory and dominant non-circulatory components in the pitching lift response superimpose to far exceed the gust-induced lift amplitudes. In contrast, for the low-frequency case with λ_g = 2.5 in Figs. 3-4(b), the gust and pitching circulatory terms are comparable while the non-circulatory pitching component becomes much smaller, with the cumulative effect explaining the much reduced differences in the resulting lift response amplitudes.

(a) (b)

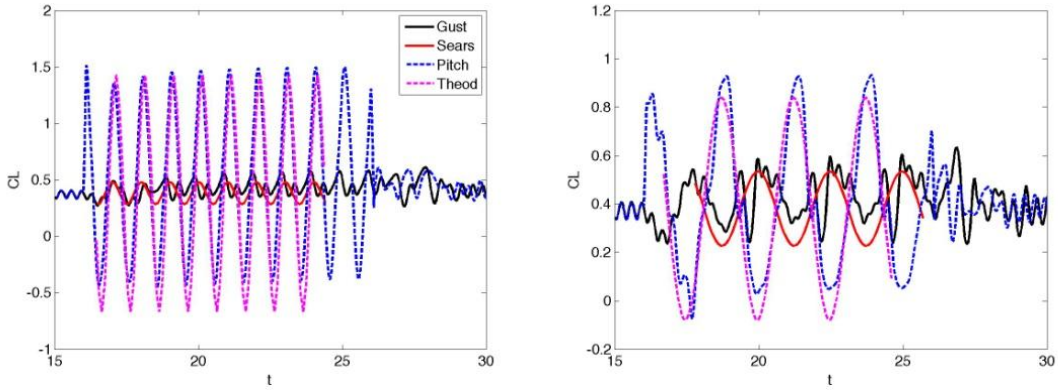

Figure 3: Airfoil response to gust vs. pitching; α_o=4^0, α_m=4^0. (a) λ_g =1, (b) λ_g =2.5.

(a) (b)

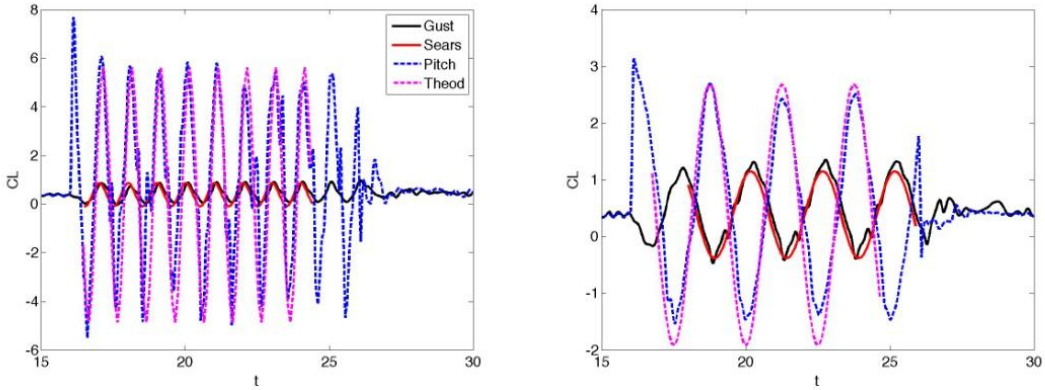

Figure 4: Airfoil response to gust vs. pitching; α_o=4^0, α_m=20^0. (a) λ_g =1, (b) λ_g =2.5.

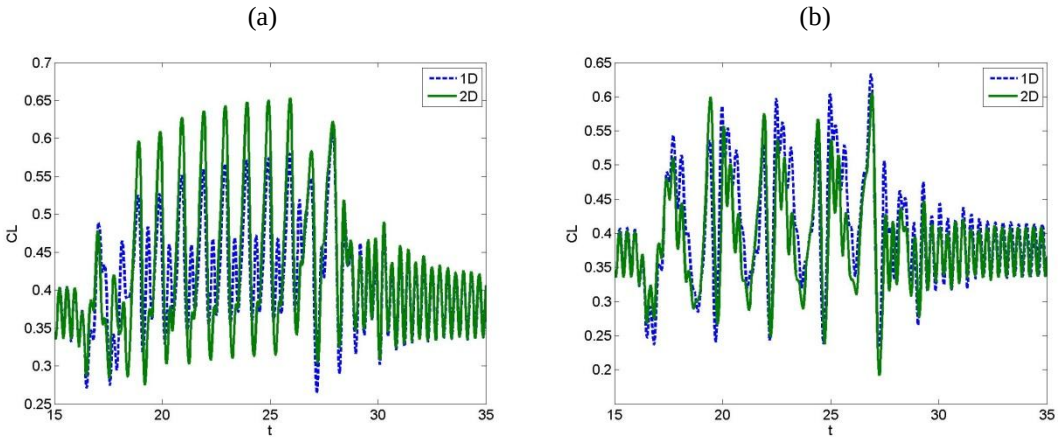

Figure 5: Airfoil response to 1D vs. 2D gust; $\alpha_o=4^0$, $\varepsilon_g=0.07$. (a) $\lambda_g=1$, (b) $\lambda_g=2.5$.

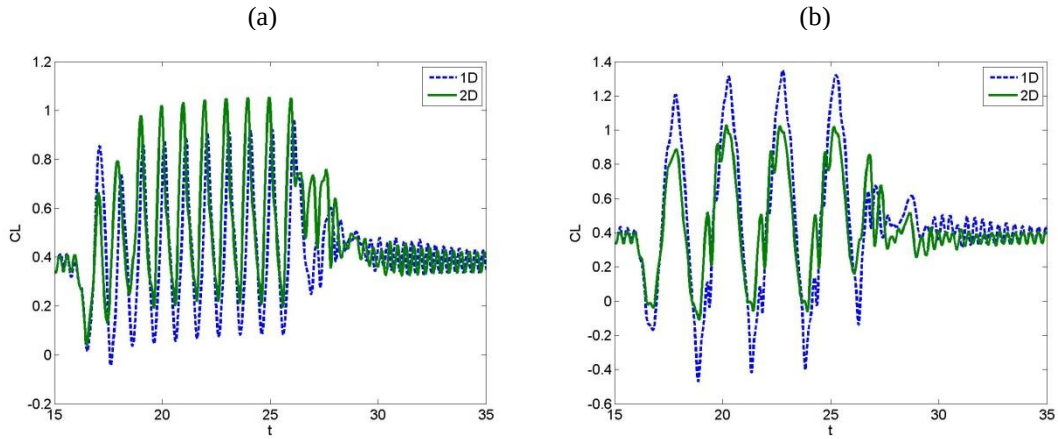

Figure 6: Airfoil response to 1D vs. 2D gust; $\alpha_o=4^0$, $\varepsilon_g=0.35$. (a) $\lambda_g=1$, (b) $\lambda_g=2.5$.

The comparison of 1D and 2D gust responses is presented in Figs. 5 and 6 for $\varepsilon_g=0.07$ and 0.35, correspondingly. For the small-amplitude excitation with more pronounced viscous effects in the aerodynamic response, the additional oscillatory streamwise velocity component in the 2D gust cases appears to contribute to a similar (for $\lambda_g=2.5$) or even larger (for $\lambda_g=1$) amplitudes of the unsteady lift despite the fact that the upwash components have actually reduced (from Eq. (3)). In contrast, for the large-amplitude cases in Fig. 6 with dominant unsteady inviscid forces, the opposite trend is noted.

5.2 Cases with $\alpha_0=8^0$

With the airfoil approaching the stall conditions, the major difference from the less-loaded airfoil cases appears in the more pronounced viscous effects observed in the airfoil response to the low-amplitude excitations (Fig. 7). The cases there reveal a less satisfactory comparison with corresponding inviscid predictions. Moreover, the examined low-amplitude cases take longer time to transition back to the original steady-state oscillations. Similar to the previous cases with $\alpha_0=4^0$, the inviscid theory shows good agreement with predicted high-amplitude lift responses in Fig. 8, although it somewhat deteriorates for the low-frequency pitching in Fig. 8(b).

The enhanced boundary-layer vortical dynamics in the case of the low-amplitude 2D gust (Fig. 9) reveals complexity of viscous effects in the unsteady aerodynamic response which does not necessarily follow the trend observed in the corresponding cases with $\alpha_0=4^0$. Note, in particular, a remarkable spike in the unsteady lift for $\lambda_g=2.5$.

For the high-amplitude cases in Fig. 10, the 2D gust airfoil response appears much stronger for the higher gust frequency (λ_g =1), while both 1D and 2D gusts produce similar responses for λ_g =2.5. Also, Figs. 10(a) and 10(b) reveal a delayed lift response following the passage of the 1D and 2D gusts, correspondingly, which is commented on further below.

(a) (b)

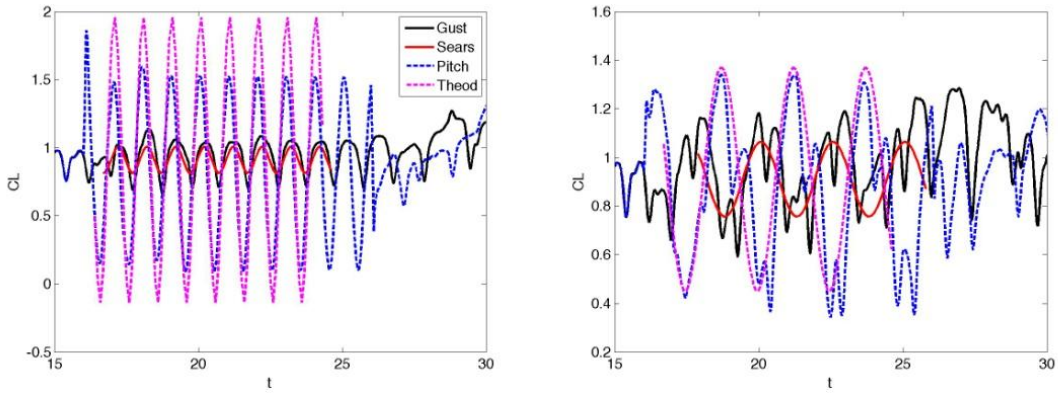

Figure 7: Airfoil response to gust vs. pitching; α_o=8^0, α_m=4^0. (a) λ_g =1, (b) λ_g =2.5.

(a) (b)

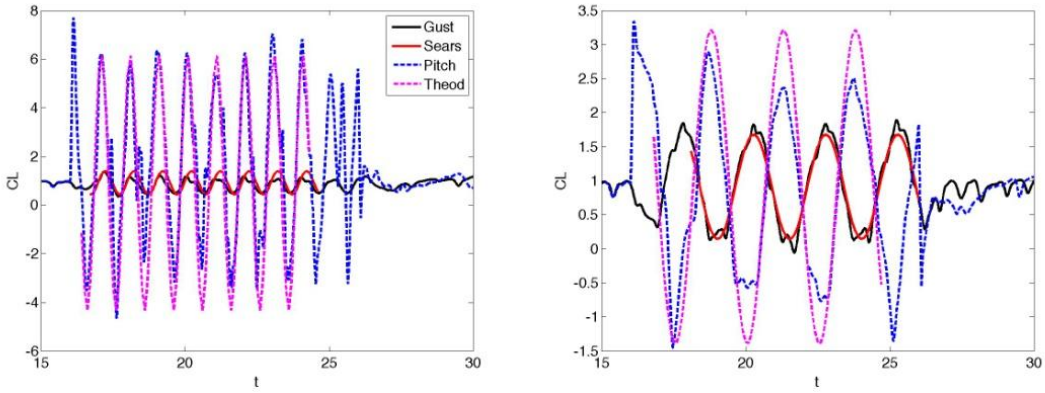

Figure 8: Airfoil response to gust vs. pitching; α_o=8^0, α_m=20^0. (a) λ_g =1, (b) λ_g =2.5.

(a) (b)

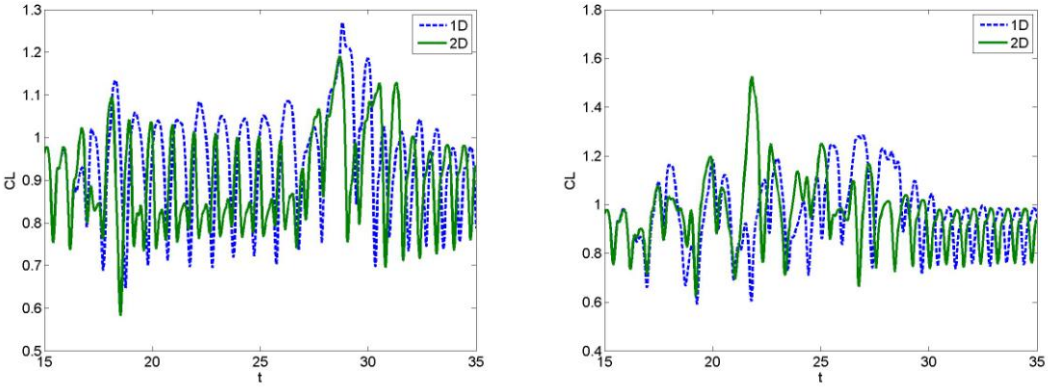

Figure 9: Airfoil response to 1D vs. 2D gust; α_o=8^0, ε_g =0.07. (a) λ_g =1, (b) λ_g =2.5.

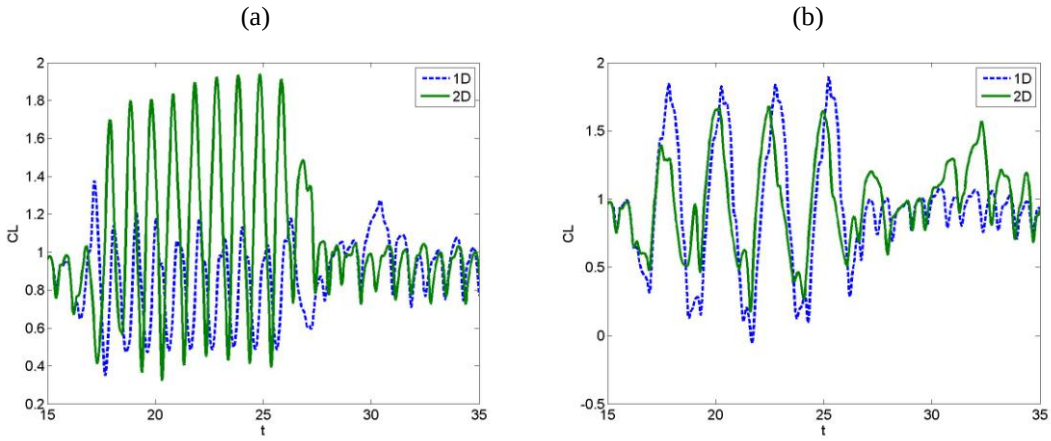

Figure 10: Airfoil response to 1D vs. 2D gust; $\alpha_o=8^0$, $\varepsilon_g=0.35$. (a) $\lambda_g=1$, (b) $\lambda_g=2.5$.

5.3 Comparison of $\alpha_0=4^0$ and 8^0 results

From the standpoint of MAV aerodynamic performance and the overall vehicle controllability, it is important to examine in more detail the change in the airfoil gust vs. pitching responses with shift in the airfoil steady loading. A comparative analysis of lift predictions obtained for $\alpha_0=4^0$ vs. $\alpha_0=8^0$ is presented here based on 1D gust simulations. For $\varepsilon_g=0.07$, the corresponding gust and pitching responses are shown in Fig. 11. Similar comparison for $\varepsilon_g=0.35$ is provided in Fig. 12. For $\lambda_g=1$, these results are further illustrated in Figs. 13-14 showing the instantaneous vorticity contours for $\alpha_0=4^0$ vs. $\alpha_0=8^0$ cases for both selected excitation amplitudes. The corresponding vorticity plots produced from gust and pitching simulations are shown side-by-side, and synchronized by showing four phases of the established cycle of induced lift oscillations corresponding to (top to bottom): average lift with increasing amplitude (C_{lo+}), maximum lift (C_{lmax}), average lift with decreasing amplitude (C_{lo-}), and minimum lift (C_{lmin}). Such comparison provides an important correlation of aerodynamic forces with dynamics of unsteady viscous flow and airfoil motion.

For the low-amplitude cases in Fig. 13, a much stronger dynamics of separated boundary layer is noted for the higher steady load. In correlation with the lift response observed in Fig. 11, the inviscid unsteady forces due to the induced vorticity shed in the wake dominate in the pitching response, while the dynamic-stall vortices convecting along the airfoil's suction side manifest the nonlinear viscous effects which appear more pronounced in the gust interaction cases. Overall, the vorticity patterns induced by pitching and gust reveal noticeable similarity.

As noted before, the viscous effects appear mainly subdued by inviscid forces in the cases of high-amplitude gust and pitching excitations, for both steady-state angles of attack. The gust-induced lift oscillations observed in Fig. 12 are identified with periodic vortex shedding in the wake as the induced upwash oscillates with the periods of observed in Fig. 14 gust vorticity waves. In the same plots, the inviscid dynamics of separated leading- and trailing-edge vortices observed for a period of pitching oscillation determines the pitching-induced aerodynamic response. With the high-amplitude airfoil motion, the vorticity contours produced in the gust and pitching response simulations hardly look alike. It is also interesting to note the airfoil position and the structure of vortices corresponding to different phases of the lift cycle in each case.

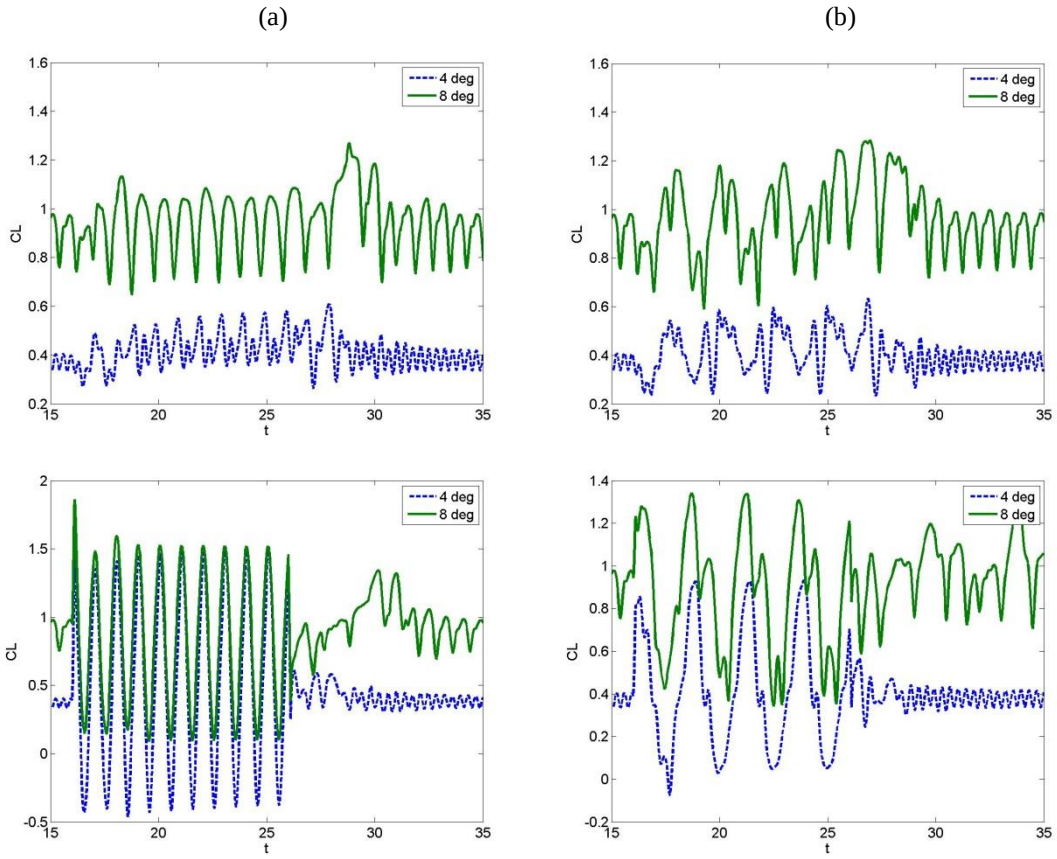

Figure 11: Airfoil response to gust (top) vs. pitching (bottom): $\alpha_o=4^0$ vs. 8^0, $\alpha_m=4^0$. (a) λ_g =1, (b) λ_g =2.5.

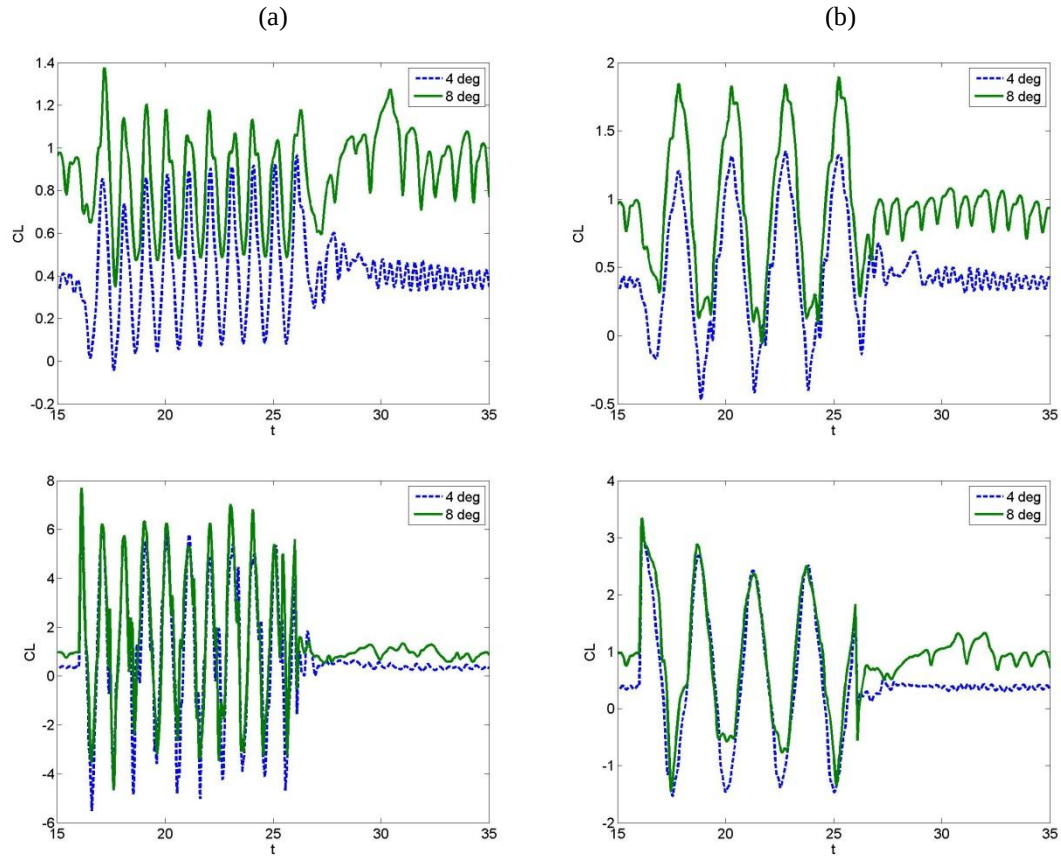

Figure 12: Airfoil response to gust (top) vs. pitching (bottom): $\alpha_o=4^0$ vs. 8^0, $\alpha_m=20^0$. (a) λ_g =1, (b) λ_g =2.5.

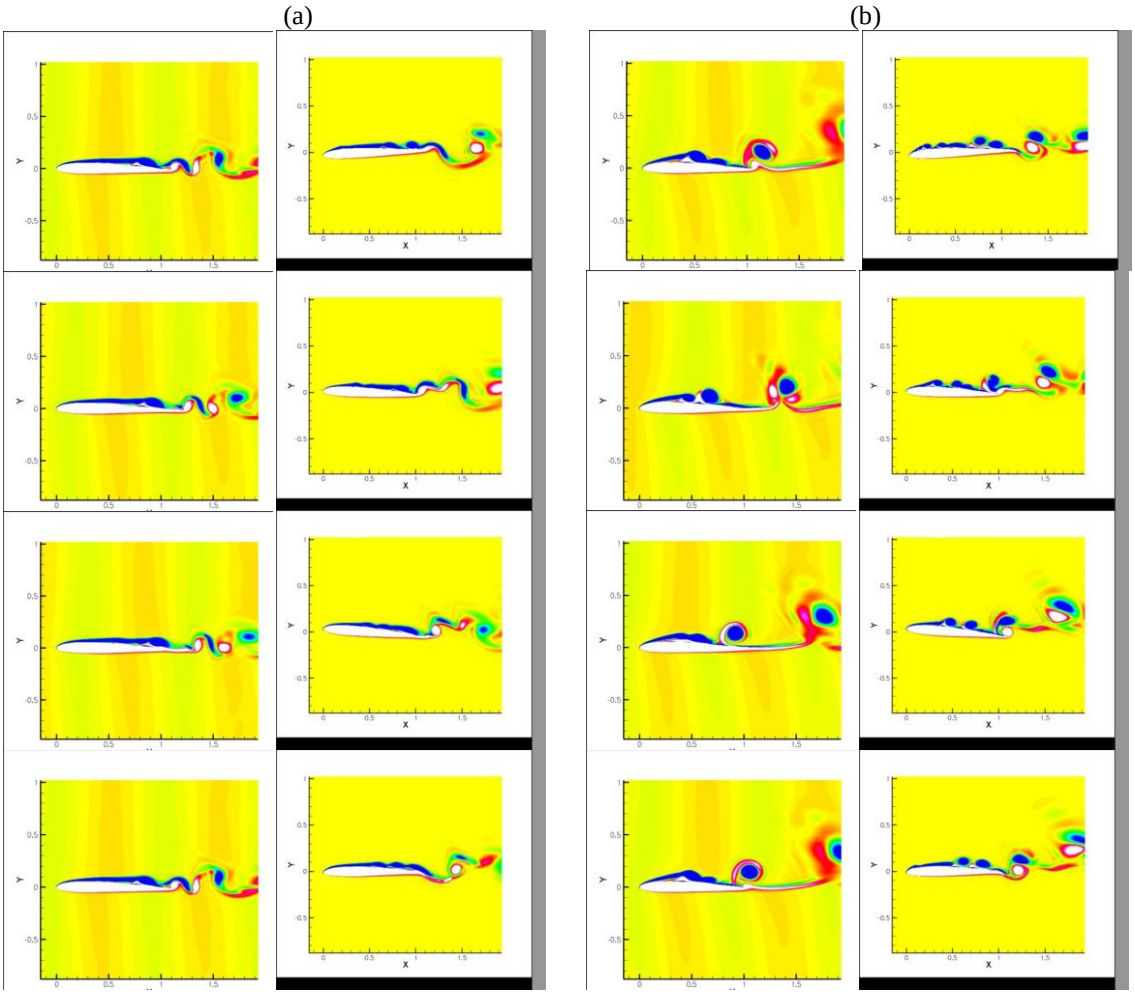

Figure 13: Vorticity contours for time-harmonic gust (left) vs. pitching (right) for a period of lift oscillation corresponding (top to bottom) to $C_{lo+,}\, C_{lmax,}\, C_{lo-,}\, C_{lmin}$; $\alpha_m=4^0$, λ_g =1. (a) $\alpha_o=4^0$, (b) $\alpha_o=8^0$.

Returning to Fig. 11, note that the comparison of the unsteady aerodynamic time histories for low-amplitude excitations points to another major difference in the airfoil responses for $\alpha_0=4^0$ and $\alpha_0=8^0$, related to the delayed aerodynamic reaction following the gust or pitching removal. For the low steady loading, the transition back to the steady-state oscillations is rather smooth and uneventful in all cases. In contrast, an intricate interplay of stronger nonlinear viscous and inviscid forces produces a much more complex airfoil reaction for $\alpha_0=8^0$. For λ_g = 1, the spikes in the aerodynamic responses are observed in Fig. 11 after $\Delta t\approx5$ and $\Delta t\approx3$ following the removal of pitching and gust excitations, respectively. Based on the numerical experiments, the observed phenomena are associated with the delayed convection of the induced boundary-layer vorticity which eventually bursts into the wake to produce the delayed aerodynamic response. On the other hand, in contrast to the gust response which eventually transitions to the steady-state fluctuations in all considered cases, the pitching response in Fig. 11 for λ_g =2.5 does not show clear signs of settling.

Commenting on Fig. 12 for the high-amplitude cases, a similar delayed reaction in the aerodynamic response is observed both for gust and pitching excitations. For the gust response, the delayed response can be seen for λ_g =1 case, whereas an uneventful transition is observed for λ_g =2.5 case.

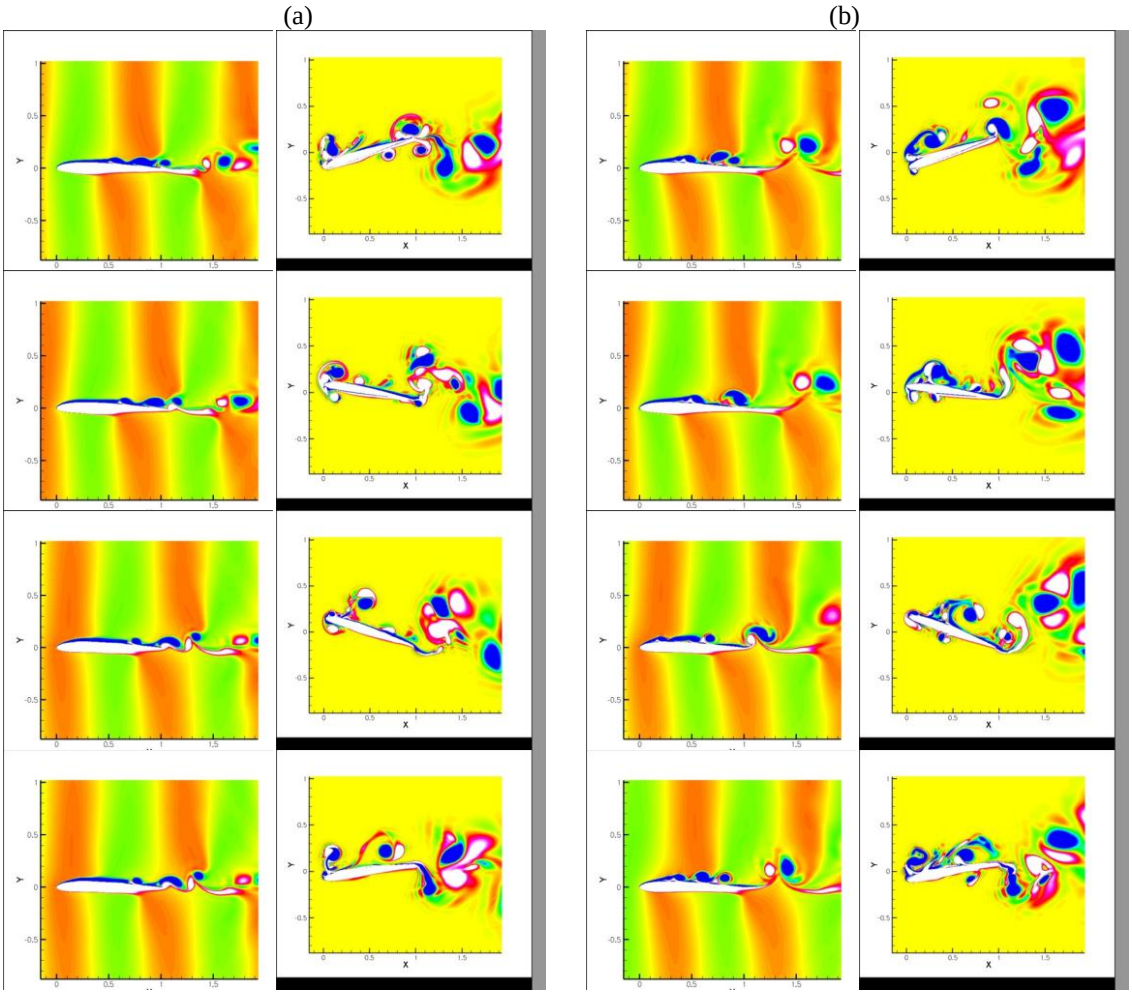

Fig. 14. Vorticity contours for time-harmonic gust (left) vs. pitching (right) for a period of lift oscillation corresponding (top to bottom) to C_{lo+}, C_{lmax}, C_{lo-}, C_{lmin}; $\alpha_m=20^0$, $\lambda_g=1$. (a) $\alpha_o=4^0$, (b) $\alpha_o=8^0$.

For the pitching response, the $\alpha_0=8^0$ cases reveal a similar initial build-up of the delayed aerodynamic reaction; however, in contrast to the small-amplitude pitching, they show eventual transition to the steady-state oscillations. Such remarkable flow regularization for the high-amplitude excitation may again be associated with the dominance of unsteady inviscid forces during the airfoil motion and following its return to the original position.

6 CONCLUSIONS

A parametric numerical study was implemented to examine the low-Re unsteady aerodynamic lift and moment responses to incident time-harmonic 1D and 2D vortical gusts. Efficient model was developed to introduce the flow perturbations inside the computational domain through the source terms in the governing momentum equations. High-accuracy Navier-Stokes simulations were conducted for SD7003 airfoil in the laminar flow regime with $M_\infty=0.1$ and Re=10,000. Two steady-state flow conditions were considered corresponding to the airfoil installed at the angles of attack $\alpha_0=4^0$ and $\alpha_0=8^0$. The gust parameters included two amplitudes of the induced angles of attack corresponding to $\alpha_m=4^0$ and 20^0.

The effects of gust amplitude and frequency on aerodynamic response were examined in comparison with results from the corresponding time-harmonic pitching analysis. The unsteady predictions were matched against theoretical inviscid solutions revealing the overall dominance of inviscid effects both in gust and pitching responses.

In agreement with the inviscid unsteady aerodynamic theory, the time-harmonic pitching responses far exceeded the gust responses for the higher excitation frequency, while the differences significantly reduced for the lower frequency. The exception was observed in the case of the low-amplitude gust interacting with the highly-loaded airfoil where the developed dynamic-stall vortices convecting along the airfoil's suction side manifested the presence of nonlinear viscous forces. A delayed aerodynamic response following the removal of excitation was noted for $\alpha_0=8^0$, and observed both in time-harmonic gust and pitching responses for both excitation amplitudes.

REFERENCES

[1] Mueller, T.J., and DeLaurier, J.D., Aerodynamics of Small Vehicles, *Annual Review of Fluid Mechanics*, Vol.35, pp.89-111, (2003)

[2] Shyy, W., Lian, Y., Tang, J., Viieru, D., and Liu, H., Aerodynamics of Low Reynolds Number Flyers, *Cambridge University Press*, (2008)

[3] Ol, M.V., Altman, A., Eldredge, J.D., Garmann, D.J., Lian, Y., Resume of the AIAA FDTC Low Reynolds Number Discussion Group's Canonical Cases, *AIAA Paper 2010-108*, (2010)

[4] Williams, D.R., Buntain, S., Quach, V., and Kerstens, W., Flow Field Structures Behind a 3D Wing in an Oscillating Freestream, *AIAA Paper 2009-3690*, (2009)

[5] Lian, Y., Numerical Study of a Flapping Airfoil in Gust Environments, AIAA *Paper 2009-3952*, (2009)

[6] Lian, Y., and Shyy, W., Laminar-Turbulent Transition of a Low Reynolds Number Rigid or Flexible Airfoil, *AIAA Journal*, Vol.45, pp. 1501-1513, (2007)

[7] Lian, Y., and Shyy, W., Aerodynamics of Low Reynolds Number Plunging Airfoil Under Gusty Environment, *AIAA Paper 2007-71*, (2007)

[8] Visbal, M.R. and Gaitonde, D.V., On the Use of High-Order Finite-Difference Schemes on Curvilinear and Deforming Meshes, *Journal of Computational Physics*, Vol. 181, pp.155–185, (2002)

[9] Anderson, D.A., Tannehill, J.C. and Pletcher, R.H., Computational Fluid Mechanics and Heat Transfer, *McGraw-Hill Book Company*, (1984)

[10] Visbal, M.R. and Rizzetta, D.P., Large-Eddy Simulation on Curvilinear Grids Using Compact Differencing and Filtering Schemes, *Journal of Fluids Engineering*, Vol. 124, pp.836–847, (2002)

[11] Visbal, M.R., Morgan, P.E. and Rizzetta, D.P., An Implicit LES Approach Based on High-Order Compact Differencing and Filtering Schemes, *AIAA Paper 2003-4098*, (2003)

[12] Lele, S.K., "Compact Finite Difference Schemes with Spectral-Like Resolution," *Journal of Computational Physics*, Vol. 103, pp. 16–42, (1992)

[13] Scott, J.R., Single Airfoil Gust Response Problem, Proceedings of the 4th CAA Workshop on Benchmark Problems, *NASA CP-2004-212954*, pp.45-48. (2004)

[14] Lockard, D.P. and Morris, P.J., Radiated Noise from Airfoils in Realistic Mean Flows, *AIAA Journal*, Vol. 36, No.6, pp. 907-914, (1998)

[15] Hixon, R., Golubev, V.V., Mankbadi, R.R., Scott, J.R., Sawyer, S. and Nallasamy, M., Application of a Nonlinear Computational Aeroacoustics Code to the Gust-Airfoil Problem, *AIAA Journal*, Vol. 44, No.2, pp. 323-328, (2006)

[16] Golubev, V.V., Mankbadi, R.R., and Hixon, R., Space-Time Mapping Analysis of Airfoil Nonlinear Interaction with Unsteady Inviscid Flow, *AIAA Journal*, Vol. 43, No.10, pp. 2147-2156, (2005)

[17] Visbal, M.R., Gordnier, R.E., and Galbraith, M.C., High-Fidelity Simulations of Moving and Flexible Airfoil at Low Reynolds Numbers, *Experiments in Fluids*, Vol. 46, pp. 903-922, (2009)

[18] Fung, Y.C., An Introduction to the Theory of Aeroelasticity, *Dover*, (1993)